ELSEVIER

Thermochimica Acta 384 (2002) 7–21

thermochimica acta

www.elsevier.com/locate/tca

Femtosecond time-resolved spectroscopy of energetic materials

Gregory P. Wakeham[1], Dutch D. Chung[2], Keith A. Nelson[*]

Massachusetts Institute of Technology, Chemistry Department, Cambridge, MA 02139, USA

Abstract

A novel single-shot femtosecond spectroscopy technique permits real-time examination of irreversible decomposition in energetic solids. In a single laser shot, measurements at 400 different temporal delays are recorded to cover a total temporal range of more than 10 ps in 30 fs steps. This is accomplished by using two crossed echelon optics to separate a single probe pulse into 400 spatially and temporally separate probe pulses. Dielectric breakdown of silica glass and of 1,3,3-trinitroazetidine (TNAZ) was observed to occur on the time scale of the 50-fs pump pulse duration. © 2002 Elsevier Science B.V. All rights reserved.

Keywords: Femtosecond time-resolved spectroscopy; Energetic materials; TNAZ (1,3,3-trinitroazetidine)

1. Introduction

Decomposition of energetic materials is a complex dynamical process involving events that span a wide range of time scales. Elementary intramolecular motions including those involved in molecular vibrations, bond breakage, and bond formation occur in tens to hundreds of femtoseconds. Elementary collective motions including those that mediate lattice vibrations, intermolecular collisions, and shock front propagation between neighboring lattice sites occur on the hundred-femtosecond time scale. While macroscopic shock front propagation, build-up of energetic primary reaction products, and detonation occur on much slower time scales, elucidation of the elementary events is crucial for an understanding of the microscopic mechanisms of energetic material decomposition.

In principle, femtosecond time-resolved spectroscopy should permit direct observation of the fast events of interest. However, there are several prerequisites that must be satisfied. The most daunting challenge is posed by the irreversible destruction of the sample during the process under study. Ultrafast spectroscopy as it is normally conducted involves the use of an excitation pulse to initiate the events of interest and a temporally delayed probe pulse to monitor the sample at a particular time after excitation. This measurement, with the probe delay time held constant, is typically repeated many time to optimize signal/noise levels. The probe delay is then changed and the repeated measurements conducted again to determine the sample response at a second delay time. This procedure is repeated with many different excitation-probe delay times until the entire time-dependent sample response is mapped out. The entire procedure typically involves many thousands or millions of excitation-probe repetitions. If the sample is a liquid or a gas, then irreversible change induced by

[*] Corresponding author.
E-mail address: kanelson@mit.edu (K.A. Nelson).
[1] Present address: Seagate Technology, 7801 Computer Ave Bloomington, MN 55435, USA.
[2] Present address: Fish & Neave, 1251 Avenue of the Americas, New York, NY 10020, USA.

0040-6031/02/$ – see front matter
PII: S0040-6031(01)00774-2

the excitation pulse can be managed through continuous flow of fresh material into the irradiated region. For a solid-state sample, however, flow is not an option. Rastering of different sample regions into the excitation-probe beam path may be practical for a highly uniform semiconductor or polymer sample, but for energetic single crystals, often obtained as small and irregular pieces, this is rarely if ever possible. Thus, new methods must be developed that provide the entire ultrafast sample response in a single laser shot. On picosecond and slower time scales, the necessary time resolution is offered through fast electronic apparatus including streak cameras and digitizing oscilloscopes. On femtosecond time scales, all-optical methods must be developed. In the present paper, we report the development of such a method and its preliminary application to the energetic material 1,3,3-trinitroazetidine (TNAZ).

Several approaches to performing single-shot femtosecond spectroscopy have been tried, including spatial [1] or spectral [2] dispersion of probe light and readout based on the resulting space-to-time or wavelength-to-time correspondence, and single-shot cross-correlation of quasi-cw probe light [3,4]. These methods are applicable to some samples, but have disadvantages including requirements for high optical quality and uniformity of the sample, high excitation or ''gate'' pulse intensity, or ambiguity between temporal and spectral responses of the sample. The use of multiple-beam splitting and reflective optics to produce several separate probe beams required excessive multiple-beam alignment and did not provide a sufficient number of probe pulses to provide high temporal resolution over a substantial time-window [5]. The apparatus describe below eliminates both of these problems through the use of glass echelon optics for generation of a large number of temporally and spatially separated probe pulses from a single input pulse [6]. The numerous probe beams allow for measurement of the temporal response of a sample following a single excitation event over a 10-ps time-window with sub-100-fs time resolution. For the present demonstration, an intense nonresonant excitation pulse was used to induce dielectric breakdown in silica glass and TNAZ. The method and the present results are of interest in the study of dielectric breakdown and high-intensity light–matter interactions as well as energetic material decomposition.

The other key prerequisites for time-resolved spectroscopy are suitable light–matter interactions through which the events of interest can be initiated by the excitation pulse and monitored by the probe pulse(s). Although, these topics will not comprise the central focus of the present paper, initiation of different crystalline responses through different nonlinear light–matter interactions and probing of the responses through different mechanisms will be illustrated and discussed.

The interaction between high-intensity light pulses and energetic materials is of interest in its own right in connection with practical applications in ultrafast laser machining of energetic materials. The single-shot spectroscopy methods demonstrated here permit direct evaluation of the time-dependent response to irradiation under conditions similar to those used in ultrafast laser micro-machining, and should be of general interest in assessing the mechanisms and the dynamical responses of importance in this emerging technology.

2. Dual-echelon single-shot apparatus

The use of a transmission (or reflection) echelon to induce an array of spatially and temporally separated probe pulses of light was first introduced [7] in the early days of picosecond lasers, when low repetition rates and large shot-to-shot fluctuations frustrated signal averaging over many repetitions as it is now conducted. The millimeter-range thickness of the echelon-steps required for picosecond delays and the limited detector arrays available at the time made the method difficult. Modern apparatus such as streak cameras and GHz oscilloscopes have rendered the use of echelons in picosecond spectroscopy obsolete even in cases that require single-shot measurement. However, these devices do not provide sufficient time resolution for femtosecond spectroscopy.

The structure of a transmission echelon optic is shown in Fig. 1a. If a pulse of light is incident on such a staircase structure, as shown in Fig. 1b, the light emerging from the thicker steps of glass will be delayed relative to the light emerging from the thinner steps since the light speed, $v = c/n$, in the glass of refractive index $n \approx 1.5$ is slower than the speed of

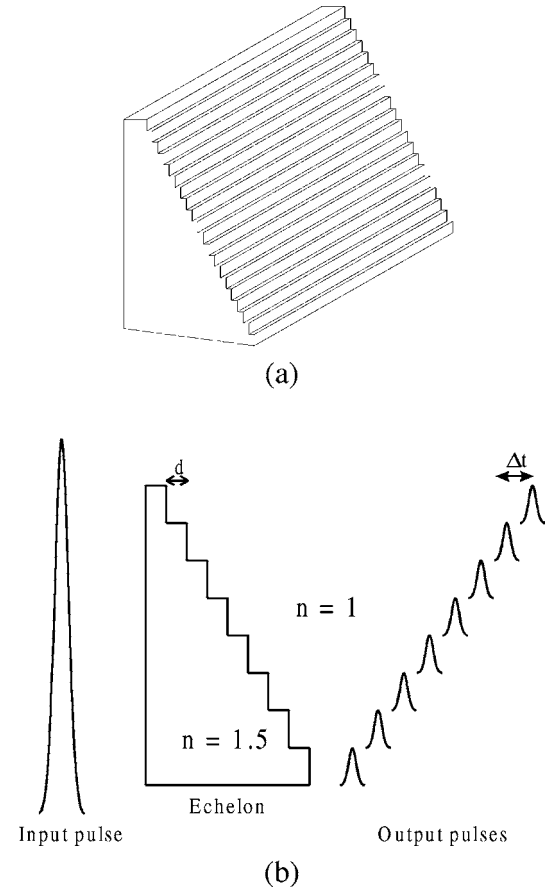

Fig. 1. (a) Schematic diagram of a transmissive echelon. (b) Generation of multiple, spatially and temporally separate pulses from a single incident pulse through the use of a transmissive echelon.

light in air. The delay introduced by a step of thickness d is

$$\Delta t = (n-1)\frac{d}{c}. \quad (1)$$

A refinement introduced here over previous echelon experiments, made possible in part by the availability of high-quality two-dimensional array detectors, is the use of two echelons to increase geometrically the number of probe beams. A single echelon with a set of s_1 steps transforms the input pulse into an array of s_1 output pulses that are spatially separated from one another along an axis transverse to the propagation direction. A second echelon with a set of s_2 steps oriented perpendicular to the first set results in a total

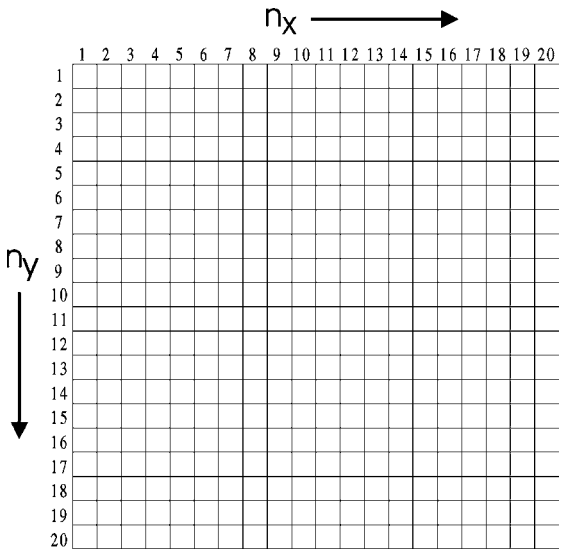

Fig. 2. Diagram of the 20 × 20-grid of probe beams formed by the two echelons. The delay time for the pulse with coordinates (x, y) is given by $[(570\text{ fs}) \times n_x + (30\ \{\ \text{fs}\}) \times n_y]$.

of $s_1 s_2$ temporally and spatially separated pulses. In our setup, each echelon has 20 steps. One of the echelons has a step size that introduces a 30-fs delay between successive pulses. This corresponds to our desired time resolution. The other echelon-step size yields a delay of 570 fs. Emerging from each of these larger steps is a strip of light that is divided into 20 square-shaped pulses, with successive pulses separated by 30 fs and with all the pulses in the strip covering a total range of 600 fs. The 20 × 20-grid of points is illustrated in Fig. 2, with the time delay for point (x, y) given by

$$\Delta t = t_x n_x + t_y n_y \quad (2)$$

with $t_{x=570}$ fs and $t_y = 30$ fs in our case. The total temporal range covered in 30-fs steps by all the pulses is 11.4 ps. This is sufficient for many measurements, and it extends well into the range that can be covered by conventional devices including a streak camera which may be used if single-shot observations must be continued out to longer time scales. The echelons step widths, and therefore, the sides of each of the 400-square probe beams, were 0.690 mm, yielding a total grid dimension of 1.38 cm (diagonal approximately 2 cm). The echelons (Diffraction Products Inc.) consist of a fused silica right-angle prism with

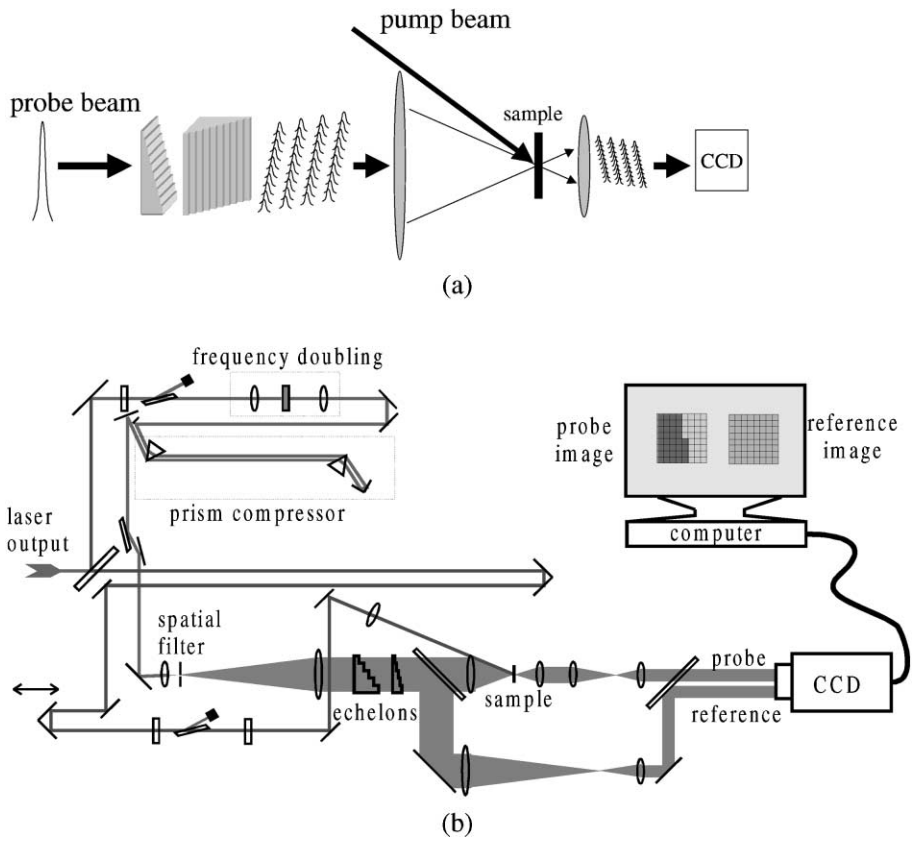

Fig. 3. (a) Simplified schematic diagram of the single-shot dual-echelon apparatus. (b) Schematic illustration of the single-shot apparatus with an 800-nm pump beam (dark lines) and a 400-nm probe beam (shaded lines).

an index-matched epoxy substrate glued onto the hypotenuse surface. The epoxy substrates were cast from metal masters that had been fabricated to have the specified step sizes.

A schematic illustration of the central experimental elements is shown in Fig. 3a. As shown, the many probe beams produced by the two echelons are focused onto the same region of the sample that is irradiated by the excitation pulse. The transmitted probe pulses are then directed toward a CCD detector at which the intensity of each beam is determined. The lenses before and after the sample form a two-lens telescope such that the grid of probe beams is focused at the sample and imaged at the detector.

Fig. 3b shows a detailed layout of the experimental apparatus. An amplified home-built titanium–sapphire laser is used as the light source. The laser operates at a center wavelength of 810 nm and produces pulses 50 fs in duration at a 10-Hz repetition rate. The output is separated into two beams, one for the pump and the other for the probe. The pump beam is passed through a small number of optical elements, resulting in preservation of the short pulse duration. A long focal length lens is used to focus the beam onto the sample so that the irradiated region is substantially larger than the probe spot size.

The optical path of the probe beam is more complex. Standard experimental methods for reduction of noise due to scattered light from the pump beam, such as periodic chopping of the probe beam and use of a phase-locked detector, are not applicable to a single-shot measurement. This is a particularly important issue with high pump intensities and induced sample damage that leads to substantial scattering even within the pump pulse duration. Therefore, different pump and probe wavelengths are used so that scattered pump

light can be filtered spectrally from the probe signal. A type 1 100 μm β-barium borate (BBO) second harmonic generation crystal is used to produce a 408-nm probe pulse.

As seen in Fig. 3b, the 408-nm probe beam is passed through many optical elements before reaching the sample. All of them can contribute to pulse broadening due to dispersion. To minimize these effects, calcium fluoride optics are used wherever possible. To reduce dispersion effects, the probe beam is passed through a prism compressor. The final pulse duration of the probe pulses at the sample is 110 fs.

After the compressor, the probe beam is passed through a beam expander/spatial filter, which consists of a 20:1-Keplerian telescope with a pinhole at the focus. The spot size of the beam is increased to over 5 cm diameter before reaching the second lens, whose diameter is 2.54 cm. A large aperture is inserted just before it to block the light that would not pass through the lens. Through transmission of only the central region, the mode of the beam is changed from gaussian to quasi-plane wave. Following the telescope, the probe beam is passed through the echelon optics. Because the mode of the beam is quasi-plane wave, the intensities of the 400-probe beams emerging from the echelons are roughly uniform. The echelons are followed by a 50%-beamsplitter which diverts half of the probe light around the sample apparatus to be used for a set of reference probe beam intensities, as described further below.

The probe light that is transmitted through the beamsplitter is passed through a two-lens telescope with the sample in the focal plane. In order to focus the beams such that greater than 90% of the beam intensity is contained within a 200-μm diameter spot, a short focal length lens (7.5 cm or less) is required. In our current setup, with the pump beam directed around this lens toward the sample, the off-axis angle of incidence of the pump beam increases as the lens focal length becomes shorter. Use of a 1-in. diameter, 7.5-cm lens to focus the probe beams onto the sample gives a minimum angle for the pump beam of $\sim 14^{\circ}$.

Another difficulty in using a short focal length lens is presented by spherical aberration. A 7.5-cm focal length with a 2-cm beam profile gives an *f*/2 of $7.5/2 = 3.25$, well beyond the distortion limit of a singlet lens. Early attempts to use such a lens resulted in focusing of the probe beams on the edges and corners of the grid to different sample regions from those to which the central beams were focused. An achromatic doublet lens provides better, though still imperfect, performance.

Diffraction and interference effects on the probe beam spatial profile at the sample must be considered carefully. Each of the 400-probe beams emerging from the echelon pair is effectively emerging from a square aperture, with the associated diffraction effects due to the echelon-step edges. Since the beam profile at the focal plane is given by the Fourier transform of the input profile, we anticipate a two-dimensional sinc^2 functional form for the spatial distribution of light at the sample. This expectation is only partially correct, however, due to interference between probe beams that are passed through adjacent steps of the thinner echelon structure. Since the pulse duration exceeds the 30-fs temporal delay between successive steps of this echelon, successive pulses are partially overlapped temporally as well as spatially, and interference can occur.

Fig. 4 shows a CCD-image of the probe beams at the sample plane. In order to permit clear observation of secondary diffraction peaks, saturation of the detector at the center of the beams has been permitted. The vertical and horizontal axes correspond respectively to the thick and thin echelon-step directions.

One-dimensional slices along each axis extracted from an unsaturated CCD-image (recorded with the beams more heavily filtered than in Fig. 4) are shown in Fig. 5. For the vertical profile (Fig. 5a), caused by the thick echelon-steps, the sinc^2 function is reasonably accurate although diffraction effects are too small to permit a critical test. In this direction the temporal delay between successive steps far exceeds the pulse duration, preventing interference effects. For the horizontal diffraction profile (Fig. 5b), caused by the thin echelon-steps, departure from the sinc^2 form is apparent. Interference between successive pulses gives rise to significant changes in the relative intensities of diffraction features. The relative intensities depend strongly on the optical phase difference between pulses emerging from neighboring steps. As shown in Fig. 5c, if the temporal delay between successive steps is an integral multiple of the optical period (i.e. the delay distance in an integral multiple of the central optical wavelength) then the intensity is concentrated almost entirely into a single central peak. Additional

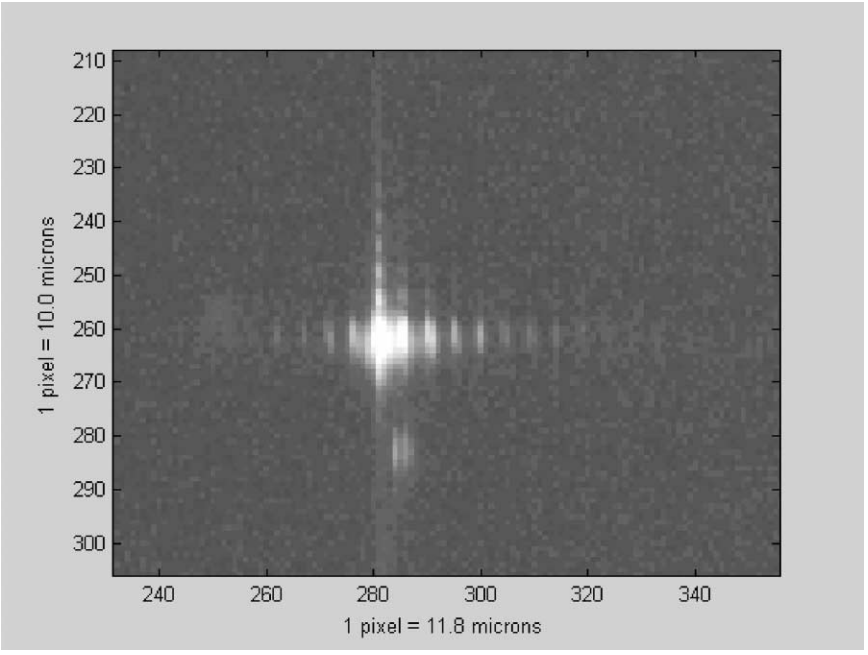

Fig. 4. CCD-image of the probe beams at the sample position. The thick echelon-steps are oriented vertically, the thin steps horizontally. Both step edges diffract probe light. In the horizontal direction, neighboring pulses are partially overlapped in time as well as position, and interference effects occur. The central peaks of the image are saturated so that the secondary diffraction features are observable in the image. There is a ghost image below and slightly to the right of the original which is neglected in the analysis.

features grow in intensity and the feature locations shift as the phase difference between successive steps increases. The simulated beam profiles in Fig. 5 were calculated numerically using the Fresnel diffraction kernel [8] with the experimental input parameters. The only adjustable parameter used was the optical phase difference between pulses along the horizontal axis.

In practical terms, the most important consideration is that essentially all of the probe light should pass through a sample region that is irradiated by the central part of the excitation pulse. This condition is ensured by an excitation spot size of at least 150 μm.

A second lens is used to collimate the probe beams after transmission through the sample. The beams are passed through a second two-lens telescope in order to optimize the imaging of the crossed echelons, of dimensions 13 mm × 13 mm, onto the 6.4 mm × 25.4 mm CCD element with a practical working distance between the final lens and the CCD. The transmitted probe beams are passed through the final 50%-beamsplitter and into the CCD detector. The reference image of the echelons is reflected onto the detector as well. Mounted onto the camera is a frequency cut-off filter which blocks scattered excitation light.

The camera used for all of the experiments was a Princeton Instruments Intensified CCD camera. The camera has a 25-mm micro-channel plate image intensifier fiber optically coupled to a 256 × 1024-pixel CCD array. The pixel size is 26 μm × 26 μm. The gating time of the intensifier can be as short as 50 ns.

The first step in acquiring the data is the recording of a signal/reference image without excitation of the sample by the pump beam. This permits accurate normalization of the signal, with any differences between signal and reference images due to sample imperfections, different optical elements and different optical paths traversed by the probe and reference beams taken into account. Signal images recorded with and without the excitation pulse are compared to evaluate the effects of the latter. Reference images

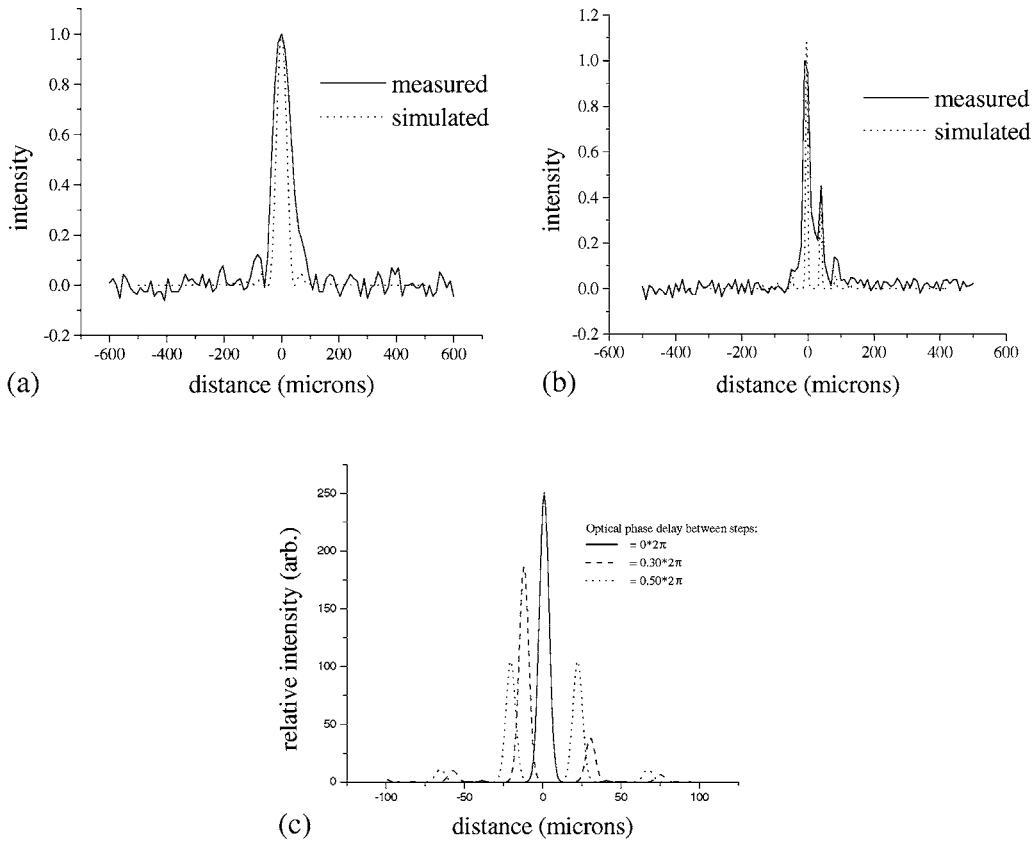

Fig. 5. (a) Vertical slice of the probe beam profile at the sample position, from an image similar to that in Fig. 4 but not saturated. A calculated profile is shown (dotted curve). The effects of diffraction by the thick step edges are minor. (b) Horizontal slice of the probe beam profile at the sample position, from an image similar to that in Fig. 4 but not saturated. A calculated profile is shown (dotted curve). The combined effects of diffraction by the thin echelon-steps and interference between neighboring pulses are substantial. The differences between the calculated profile (dotted curve) and the actual interference pattern arise from imperfect focusing of all the beams to one sample spot and from slight variations across the echelon of the phase difference between adjacent steps. (c) Calculated probe beam profiles in the horizontal direction, showing interference patterns between neighboring beams as a function of the optical phase difference between them. If the phase delay is an exact multiple of the optical period, then a single peak predominates. For other phase delays, multiple peaks of substantial intensity are observed.

recorded with and without the excitation pulse are compared to account for the effects of any shot-to-shot beam pointing instability or mode fluctuations.

3. Results and discussion

Results are presented for a silica glass sample, which at high excitation intensities undergoes dielectric breakdown without the additional complexity of molecular reaction and decomposition, and for the energetic crystal TNAZ. The responses observed in glass provide a convenient baseline for understanding the TNAZ signals, especially at high intensities.

3.1. Glass

3.1.1. Low excitation intensity

Fig. 6a shows an image recorded with the single-shot dual-echelon apparatus. The left-hand (“signal”) image of the echelons was produced by probe light that passed through a sample of fused silica glass. The intensity of 810 nm, 50 fs excitation pulse (spot diameter 130 μm) was 5 TW cm^{-2}, well below the

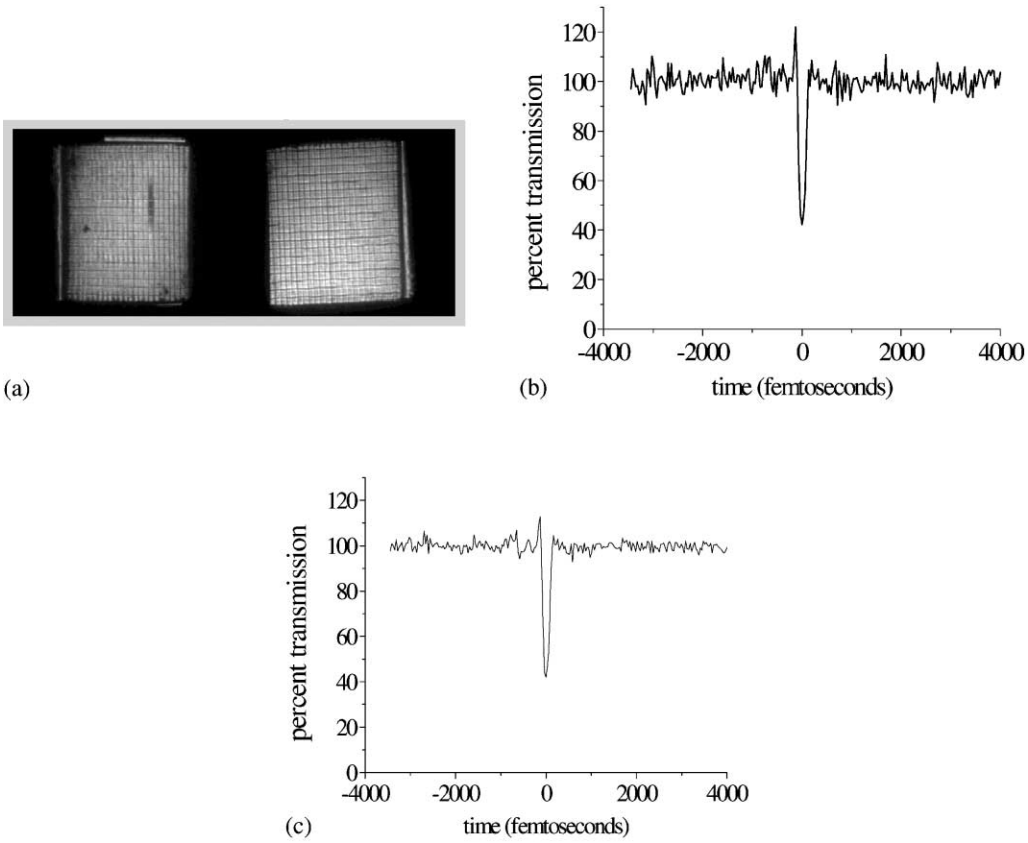

Fig. 6. (a) CCD output showing raw data from the dual-echelon single-shot apparatus with 810-nm excitation light and 408-nm probe light which passes through an interference filter centered at 403 nm before reaching the sample. The 20 × 20-grid of probe beams is apparent. The image on the left is the signal image. The thin (30 fs) steps run vertically, from bottom (shorter time delays) to top (longer delays), while the thicker (570 fs) steps run horizontally from right to left. The reference image on the right is inverted relative to the signal image, i.e. the 30-fs steps run from top to bottom and the 570-fs steps from left to right. Both images are part of a single CCD output recorded from one laser shot. The sample was fused silica glass, and the excitation pulse intensity was 5 TW cm^{-2}, well below the damage threshold. A single vertical region of the signal image shows first a very brief increase, then a longer-lived but still brief decrease, in probe light transmitted through the interference filter. This indicates a short-lived refractive index change induced by the excitation pulse, which gives rise to blue-shifting and then red-shifting of the probe pulse spectrum. (b) Processed data from a single-shot measurement on fused silica glass, showing probe transmission through the sample and interference filter as a function of time. The transient increase and decrease in probe transmission confirm the features that are apparent in the signal image of part (a). The single-shot signal intensity S.D. is ±4%. (c) Processed data as in (b) averaged over four measurements. The noise level is reduced to ±2%.

threshold for dielectric breakdown or other damage. The right-hand (''reference'') image was generated by the reference beams that bypassed the sample. The images are inverted because the probe beams were passed through a second two-lens telescope and the reference beams were not. The vertical dimension corresponds to the thinner echelon-steps, with temporal delay increasing from bottom to top in the signal image (from top to bottom in the reference image), and the horizontal dimension corresponds to the thicker echelon-steps with temporal delay increasing from right to left in the signal image (from left to right in the reference image).

In this case, the effect of the excitation light field is to induce a transient change in the silica refractive index due to both nonresonant electronic and ionic responses of the sample [9]. The short-lived sample response is evident in the signal image, which shows a

darkened region that includes approximately five steps in a single vertical column. This shows that the duration of the response is roughly 150 fs. The time-dependent changes in refractive index do not produ ce changes in probe light transmission through the sample, but they do produce shifts in the spectrum of the probe pulse. An interference filter whose 3-nm transmission curve is centered at 403 nm, on the blue side of the probe pulse spectrum (408-nm central wavelength, 8-nm bandwidth), is inserted after the sample and the probe transmission through this filter is what is measured by the images in Fig. 6a. As the probe pulse spectrum is shifted first toward the blue and then toward the red, the amount of probe light transmitted through the interference filter first increases above then decreases below the unshifted probe transmission level. This behavior is shown in Fig. 6b, which displays the normalized signal level as a function of time based on the images in Fig. 6a and the corresponding images recorded with no excitation pulse. A careful examination of the signal image in Fig. 6a reveals 1-2 brightened steps prior to (i.e. directly underneath) the darkened regions, corresponding to the initial, short-lived increase in probe transmission prior to the stronger decrease which persists for slightly longer.

The noise level in Fig. 6b at times far earlier or far later than the arrival time of the excitation pulse at $t = 0$ is approximately 4% of the total signal level. Fig. 6c shows the average of four shots, with the noise level reduced by approximately half as expected. Suggestions for experimental improvements to reduce noise are given subsequently.

The mechanisms through which the excitation light induces nonresonant electronic responses and ionic responses (i.e. motions of nuclei) in fused silica are worth careful consideration since they come into play in organic molecular crystals as well. Both sample responses are proportional to the square of the excitation field amplitude. The electronic response is due to partial saturation of the linear polarization, i.e. at some intensity, the electronic polarization is no longer linear in the field amplitude but rather has higher-order terms that become significant. Since the nonresonant electronic dynamics are essentially instantaneous, the electronic response follows the excitation pulse profile and the resulting change in refractive index is simply

$$\Delta n_{\mathrm{elec}}(t) = n_2 I_{\mathrm{e}}(t) \tag{3}$$

where $I_{\mathrm{e}}(t)$ is the excitation pulse temporal profile and n_2, the nonlinear refractive index, is a small positive number. The excitation intensity profile first increases to its maximum value, then decreases, and the refractive index follows this behavior. The induced probe spectral shift is given by the time-derivative of the refractive index change, i.e. the probe spectrum is shifted toward the blue as the excitation pulse enters the sample and toward the red as the excitation pulse leaves. This produces an increase and then a decrease in probe transmission through the interference filter.

The second mechanism, known as impulsive stimulated Raman scattering (ISRS) [10,11], is essentially an electrostrictive driving force exerted on the ions by the excitation light. In the limit of extremely short excitation pulse duration (i.e. short compared to the oscillation periods of local interionic vibrations in the silica), the pulse would exert an ''impulse'' driving force along Raman-active modes and coherent oscillations would follow. In the present case, the broad low-frequency Raman spectrum of the glass indicates many localized vibrational frequencies, most too high for the excitation pulse duration to be in the impulsive limit. In this case an ionic response which follows the excitation pulse temporal profile with some lag (described by the convolution of the excitation pulse profile with the multi-frequency vibrational response functions), and which shows little or no oscillatory character after the pulse leaves the sample, is still driven. The convolution of the electronic and ionic driving forces and responses with the probe pulse duration results in data of the form shown in Fig. 6.

3.1.2. High excitation intensity

At high excitation intensity levels, the sample undergoes dielectric breakdown, permanent structural damage, and ablation, resulting in dramatic changes in optical absorption and scattering levels. Sample responses over a range of time scales were probed with the dual-echelon technique and with a streak camera.

Fig. 7 shows the transient response of fused silica recorded with the same probe pulse and interference filter parameters as in Fig. 6 and with the same excitation pulse parameters except the intensity of 78 TW cm^{-2} (pulse energy 530 μJ) which is far above the sample damage threshold of approximately 60 TW cm^{-2} [12] for a 50-fs pulse. The signal image shows a precipitous drop during the excitation period,

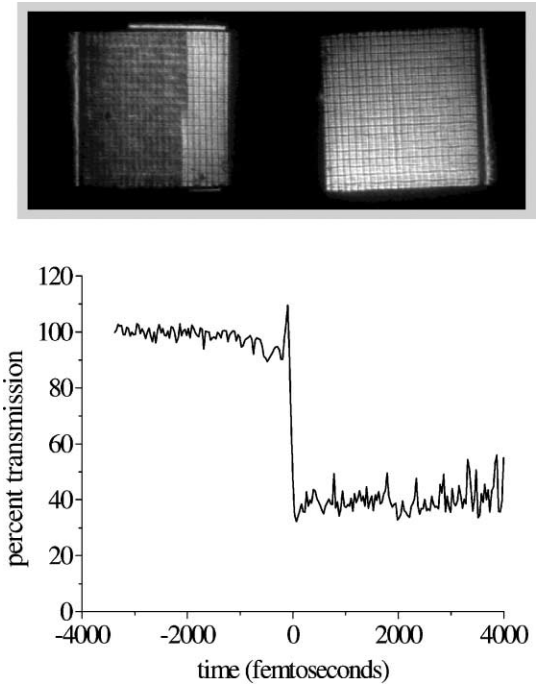

Fig. 7. CCD signal and reference single-shot images and processed data (average of five measurements) from fused silica glass with an 810-nm excitation pulse whose intensity is 78 TW cm^{-2}, far above the dielectric breakdown threshold. The transmitted probe light intensity is abruptly reduced upon arrival of the excitation pulse, with little or no subsequent change, indicating nearly instantaneous initiation of permanent sample damage.

followed by almost no subsequent change. In this case, the excitation pulse generates a high density plasma (on the order of 10^{20} electrons per cm^3) within a thin (less than 1 μm) region near the surface [12–15]. The plasma quickly relaxes [16], transferring energy to the lattice modes (using that term in the case of the amorphous solid to refer to the localized interionic vibrations as well as the collective vibrations) of the material. The lattice overheats, causing the thin layer of excited material to ablate from the surface within a nanosecond [17]. The data in Fig. 7 indicate that initiation of sample decomposition occurs within the temporal resolution of the measurement (125 fs). This result appears to be in conflict with theoretical expectations that indicate slower transfer of energy from the electrons to the lattice.

The reduced signal at long times is due to reduced transmission through the sample, not through the interference filter, since probe spectral shifts due to dynamic change in the sample refractive index are long finished. The sample damage and reduced probe transmission are permanent.

3.2. TNAZ

We can now compare the results from fused silica to those obtained from TNAZ. The crystals used in the present experiments were grown by sublimation. Typical dimensions were 3 mm × 0.4 mm × 1 mm along the *a*, *b*, and *c* axes respectively. All measurements were performed with the beams entering and leaving through the [0 1 0] face.

3.2.1. Low excitation intensity

3.2.1.1. kHz repetition rate. Although TNAZ undergoes rapid photodecomposition at high excitation intensities, repeated irradiation at low intensities with nonresonant wavelengths is possible with little or no sample damage. To assess the low-intensity response, femtosecond spectroscopy measurements were conducted in the conventional manner. An amplified titanium–sapphire laser system operating at a 1-kHz repetition rate was used to generate 800-nm, 50-fs pulses, and a partial reflector was used to separate the excitation pulse from the single probe pulse which was variably delayed along a stepping motorized delay line. An interference filter was placed after the sample to permit measurement of probe spectral shifts induced by the sample response.

The data are shown in Fig. 8. TNAZ, unlike an amorphous solid, has a small number of well-defined lattice vibrational (optic phonon) modes. The Raman-active modes of sufficiently low frequency are driven impulsively through ISRS by the excitation pulse. The resulting coherent lattice vibrational oscillations give rise to time-dependent changes in the refractive index and to time-dependent probe spectral shifts, as shown in the data. As in conventional Raman spectroscopy, the excitation and probe polarizations can be varied to select different Raman-active modes.

Raman studies [18,19] have shown that crystalline TNAZ has several low frequency Raman active modes at $\bar{\nu} = 85$, 124, 205, and 352 cm^{-1}. The 124 and 205 cm^{-1} modes are observed in the ISRS data, with

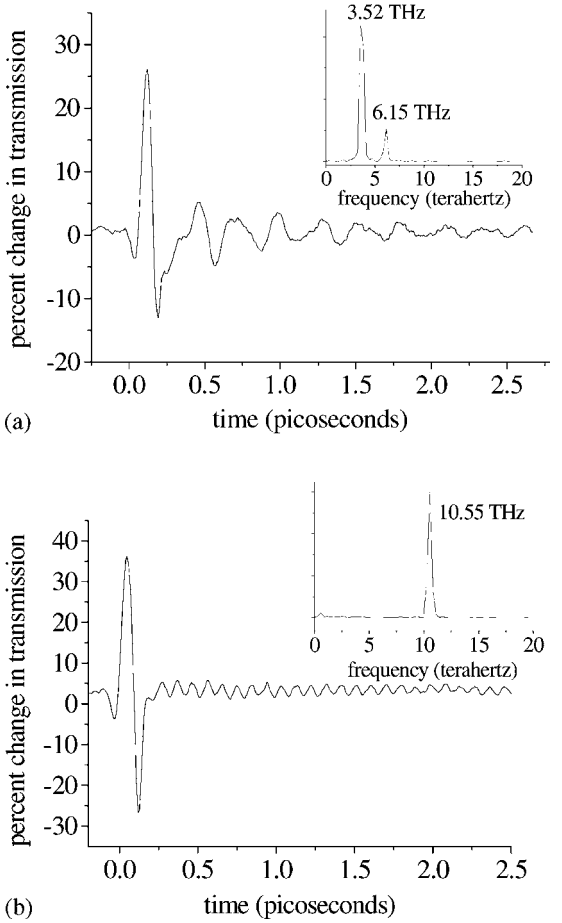

Fig. 8. (a) Pump-probe signal from TNAZ single crystal collected at a 1-kHz repetition rate with pump and probe beams parallel to the crystallographic *a*-axis. The spike at $t = 0$ is a nonresonant electronic response, as seen in the glass samples. Lattice vibrational oscillations driven through ISRS are observed at later times. (b) Pump-probe signal from TNAZ single crystal collected at a 1-kHz repetition rate with pump and probe beams parallel to the crystallographic *c*-axis. A different optic phonon mode is Raman-active with this polarization selection.

dephasing rates of 3.8 ± 2.2 ps and 740 ± 180 fs respectively, when both pulse polarizations are oriented parallel to the crystallographic *a*-axis. The 352 cm^{-1} mode is observed, with a dephasing rate of 2.4 ± 0.2 ps, when both pulse polarizations are oriented parallel to the *c*-axis.

In addition to the lattice vibrational response, each data sweep clearly shows a nonresonant electronic response at the early times.

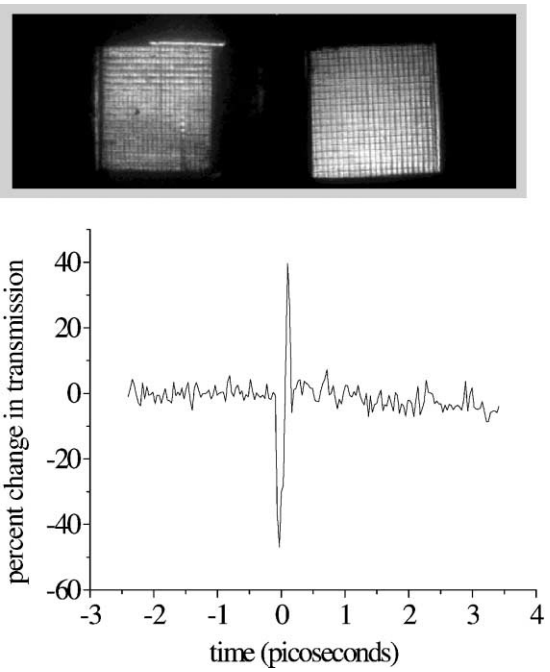

Fig. 9. CCD output showing single-shot data from TNAZ, and processed data (averaged over 10 laser shots) showing transmitted probe light through a 403-nm interference filter as a function of time. The excitation intensity is 400 GW cm^{-2}, far below the damage threshold. Only a nonresonant electronic response is observable. Coherent vibrational oscillations are presumably obscured by noise in the data.

3.2.1.2. Single-shot measurement. Fig. 9 shows single-shot transient data from TNAZ using the dual-echelon apparatus. As before, the pump beam had a central wavelength of 810 nm and the probe beam had a central wavelength of 408 nm. A 405.4-nm bandpass filter with FWHM bandwidth of 3 nm was used in front of the ICCD camera to allow detection of probe spectral shifts. The polarizations of the pump and probe beams were parallel to the *a*-axis of the crystal. Fig. 9 includes a plot of the transient response to an excitation intensity of 400 GW cm^{-2}, averaged over 10 shots. The data clearly show a nonresonant electronic response induced by the excitation pulse. There is no further signal observable above the noise level. Since the lattice vibrational oscillations observed in measurements at kHz repetition rates gave rise to signal levels similar to the present noise level, it is not surprising that oscillations are not observed in the data. The

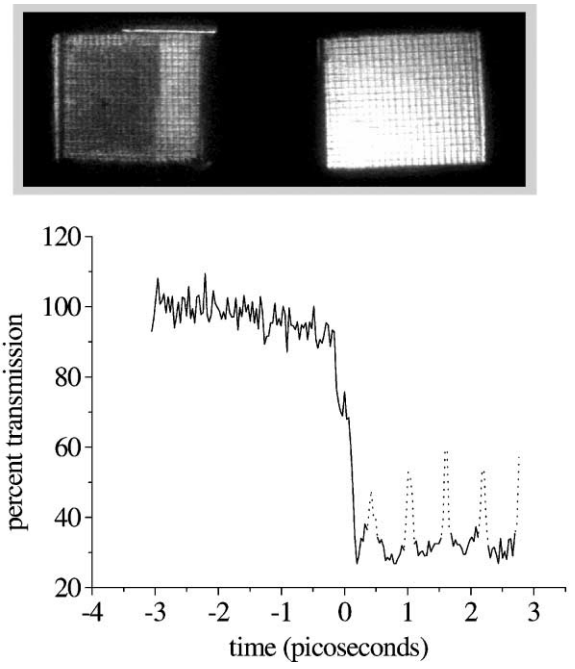

Fig. 10. CCD output showing single-shot data from TNAZ, and processed data (averaged over four laser shots) showing transmitted probe light through a 403-nm interference filter as a function of time. The excitation intensity is 22.8 TW cm^{-2}, well above the damage threshold. A sudden decrease in probe transmission is observed upon arrival of the excitation pulse, followed by little or no subsequent change on the time scale of the measurement. The focusing of probe beams near the echelon edges is poor due to spherical aberration, resulting in poor overlap between those beams and the excitation beam. This gives rise to higher transmission of those probe beams than of the others after $t = 0$ (see brighter signal image regions at top, bottom, and right-hand edges). The unreliable data points are shown as dotted curves in the plot.

excitation intensities used in the kHz measurements were comparable to those used here, typically limited by white-light generation in the sample.

3.2.2. High excitation intensity

Fig. 10 shows CCD-images from a single-shot measurement in TNAZ with an excitation intensity of 22.8 TW cm^{-2}, along with a plot of the transient response averaged over four iterations. An experimental artifact is observed in the $t > 0$ signal in Fig. 10. Imperfect focusing of the probe beams near the edges of the 20 × 20-grid due to spherical aberration caused poor overlap between these beams and the pump beam. The effect is clearly observed in the CCD signal image. A dramatic reduction of probe light is apparent after the arrival of the excitation pulse, except for the regions near the edges of the grid. Part of the light in the probe pulses corresponding to these regions passed through sample regions that were not irradiated by the intense excitation pulse, and this probe light was transmitted through the sample to the CCD detector. The strongly affected points are included in the plot below the CCD-images in Fig. 10, but they are shown connected by dotted lines to indicate the unreliability of their values. The conclusion that can be drawn reliably from Fig. 10 is that there is an abrupt reduction in transmitted probe light upon arrival of the excitation pulse and that there is no strong change in signal level thereafter on the time scale of the measurement. The possibility of coherent vibrational oscillations or other more subtle features of the time-dependent response cannot be evaluated on the basis of the data. Since the excitation intensity is more than 50 times higher than that used for the data shown in Fig. 9, vibrational oscillations (whose amplitudes should increase linearly with intensity) might be expected to give rise to far stronger signals. Rapid photoionization should also provide an impulsive driving force on lattice vibrations. However, decomposition of the lattice may destroy all vibrational coherence within the first oscillation period. Improved single-shot measurements will be needed to assess the details of the sample response on femtosecond time scales.

The fast drop-off in transmitted signal intensity is indicative of a similar initial excitation mechanism to that seen in fused silica. A plasma is generated, followed by rapid energy transfer from the excited electrons to the vibrational motions of the atoms. The lattice is quickly heated to vibrational temperatures high enough to cause structural rearrangement and vaporization. A difference, however, is seen in the intensity threshold needed to cause damage. The intensity needed to cause the response seen in Fig. 10 is approximately 1/3 of that necessary to see the same response in fused silica. It might be speculated that TNAZ has a lower ionization potential than fused silica, but this is not the case. The ionization potential of TNAZ [20] is 10.35 eV, compared to 9 eV for fused silica. The likely cause of the reduction in damage threshold is more facile plasma generation due to resonance enhancement of the multiphoton ionization rate via an intermediate electronic excited-state. The absorption spectrum of

TNAZ in ethanol shows that the lowest electronic excited-state absorption occurs at a wavelength of ∼250 nm. This broad peak extends into the spectral region of the third harmonic wavelength of the Ti:sapphire output at ∼270 nm. Therefore, a three-photon absorption process gives rise to an electronic excited-state in TNAZ, whereas for fused silica the lowest-order strongly resonant process requires four photons to reach absorption features that extend to the 200-nm range.

Fig. 11 shows single-shot transient transmission data from TNAZ on picosecond and nanosecond time scales, recorded using a Hamamatsu model C5680 streak camera. A 50-fs, 810-nm, 300-μJ pump pulse focused to a spot size of 40 μm diameter was used. This corresponds to a peak intensity of approximately 480 TW cm^{-2}. The 600-MW cw probe beam was derived from a frequency-doubled Nd–YVO_4 laser, shuttered to give a quasi-cw pulse of 5 ms duration, and focused to a spot size of 30 μm. Time-dependent transmission of the probe beam through the sample is measured.

The streak camera data show an abrupt drop-off in transmission that is temporally limited only by the (picosecond) resolution of the apparatus. There is a further decay of transmission during the first nanosecond after the arrival of excitation pulse. After this, a slower exponential decay of the transmission reduces the signal to less than a few percent within 25 ns. We note that these streak camera results are in contrast to those obtained by us from a zinc titania glass sample (not shown in the present paper), in which the very rapid decay in signal during the excitation pulse was followed by very little subsequent change (in fact only a slight increase) in probe transmission all the way out to many-nanosecond time scales.

Thermally activated decomposition is likely the cause of the decay in transmission seen at long times in Fig. 11. Unlike titania or silica glass samples, whose continuous networks of silicon–oxygen or titania–oxygen bonds have no thermally activated chemistry that can occur at moderately elevated temperatures, TNAZ, composed of individual molecules of high chemical potential energy bound together by weak intermolecular forces, melts at 100 °C and undergoes molecular decomposition above 160 °C [21]. While most of the energy absorbed from the pump pulse is kept within the first micron layer due to absorption by the plasma and subsequent ablation, some heat is transferred to the

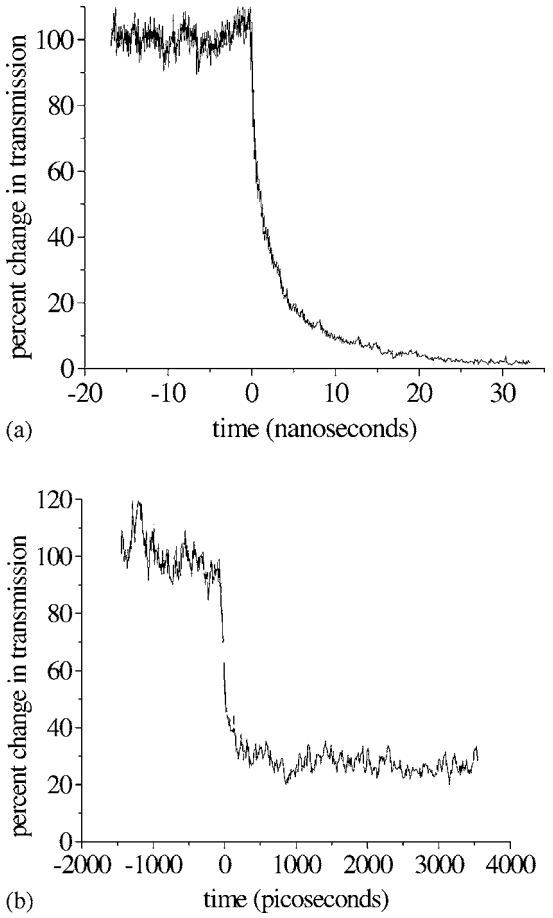

Fig. 11. Streak camera data from TNAZ showing transient transmission of quasi-cw 532-nm probe light, with a 50-fs, 800-nm excitation pulse whose intensity is 480 TW cm^{-2}, far above the damage threshold. The data show continued decay of probe transmission through the sample on a nanosecond time scale, revealing thermal decomposition subsequent to the initial damage and ablation events. The results shown in (a) are averaged over six shots and in (b) are averaged over eight shots.

underlying layer as the material decomposes and vaporizes. This heating of the sub-ablated region in TNAZ is likely to cause melting as well as molecular fragmentation, leading to surface and near surface irregularities that scatter light. Consistent with this view, it was noted by optical inspection that the light scattering level from TNAZ samples after high-intensity excitation and permanent damage was far higher than that from similarly damaged glass samples.

Finally, we note that in preliminary experiments, TNAZ crystals were exposed to 30-fs pulses of intensity

greater than 200 TW cm^{-2} at a repetition rate of 1 kHz. The duration of irradiation varied, but typically several hundred pulses were used. A violent response was observed, characterized by evaporation of the irradiated region, emission of smoke, movement of the entire crystal, and sometimes loud audible noise. The lack of real-time spectroscopic capabilities precluded any detailed analysis of this response. With our current experimental capabilities, we have not observed explosive responses in TNAZ on a single-shot basis. It is likely that the responses observed earlier depended on a build-up of reaction products and/or crystal irregularities produced by many excitation pulses. Since our time-resolved observations indicate extremely rapid decomposition and ablation upon intense irradiation, they suggest that most of the excitation pulse energy (which is absorbed within the first micron of the sample) leaves with the ejected material long before thermal diffusion is able to heat a substantial volume of the underlying sample. Since the bulk of the sample is exposed to only a small fraction of the initial pump excitation, it is not surprising that extensive reaction requires multiple excitation events.

4. Summary

A novel single-shot dual-echelon femtosecond spectroscopy method has been introduced and applied for the first time to energetic crystalline solids. The method permits real-time spectroscopic observation of permanent chemical and structural change in the solid-state, without the need for sample replenishment or flow.

Measurements on fused silica glass irradiated beyond the dielectric breakdown threshold with an intense excitation pulse revealed that permanent decomposition of the sample occurred on a time scale comparable to the 50-fs excitation pulse duration. Little or no subsequent change was observed, indicating extremely fast transfer of energy from the initially excited electron plasma to the lattice modes whose motions give rise to decomposition.

Measurements on TNAZ single crystals revealed similar results. Rapid decomposition, within the pulse duration, was observed, with no substantial additional response on femtosecond time scales. Coherent lattice vibrations, observed in high-repetition-rate measurements on TNAZ following low-intensity excitation, were not observed, although limitations in signal/noise ratio and imperfections in the focusing of multiple probe beams for the single-shot measurement preclude a definitive evaluation of the results in terms of rapid vibrational dephasing. The single-shot measurements did not provide additional observations of violent ''microexplosions'' reported in TNAZ crystals following irradiation by many intense pulses at a kHz repetition rate.

Streak camera measurements on TNAZ revealed further decomposition on nanosecond time scales. This is believed to be due to thermally induced melting and decomposition of material just beneath the thin sample region that absorbs most of the intense excitation light and undergoes rapid decomposition and ablation. The additional decomposition leads to high levels of light scattering, preventing almost all probe light transmission to a detector behind the sample.

Several important improvements to the single-shot measurement are under way. In the present setup, the primary source of noise arises from electronic amplification of signal in the intensified CCD detector. Since the probe light level is high, amplification is not necessary and this source of noise can be eliminated. Additional improvements in the speed and reliability of data reduction should lead to higher signal/noise ratios as well. We expect that single-shot noise levels substantially less than 1% should be reached. This will permit far more detailed analysis of irreversible ultrafast processes in solids. Finally, extension of the method to new probe wavelength ranges including the mid-infrared range will allow additional information, including the time-evolution of molecular vibrational frequencies and chemical composition, to be extracted.

Acknowledgements

This work was supported in part by the US. Office of Naval Research Grant N00014-96-1-1038.

References

[1] L. Dhar, J.T. Fourkas, K.A. Nelson, Opt. Lett. 19 (1994) 643–645.
[2] Z.P. Jiang, X.C. Zhang, Appl. Phys. Lett. 72 (1998) 1945–1947.

[3] W. Wang, D.D. Chung, J.T. Fourkas, L. Dhar, K.A. Nelson, J. de Phys. 4 (C4) (1995) 289–296.
[4] D.D. Chung, Ph.D. Thesis, Massachusetts Institute of Technology, MA, 1998.
[5] W. Wang, Ph.D. Thesis, Massachusetts Institute of Technology, MA, 1995.
[6] G.P. Wakeham, K.A. Nelson, Opt. Lett. 25 (2000) 505–507.
[7] M.R. Topp, P.M. Rentzepis, R.P. Jones, J. Appl. Phys. 42 (1971) 3415–3419.
[8] H. Haus, Waves and Fields in Optoelectronics, Prentice-Hall Inc., Englewood Cliffs, NJ, 1984, pp. 81–107.
[9] M.J. Banet, K.A. Nelson, Solid-state Ionics III, in: G.-A. Nazri, J.-M. Tarascon, M. Armand (Eds.), Mater. Res. Symp. Proc. 293 (1993) 437–441.
[10] Y.-X. Yan, E.B. Gamble, K.A. Nelson, J. Chem. Phys. 83 (1985) 5391–5399.
[11] Y.X. Yan, K.A. Nelson, J. Chem. Phys. 87 (1987) 6240–6256.
[12] A.C. Tien, S. Backus, H. Kapteyn, M. Murnane, G. Mourou, Phys. Rev. Lett. 82 (1999) 3883–3886.
[13] D. Du, X. Liu, G. Korn, J. Squier, G. Mourou, Appl. Phys. Lett. 64 (1994) 3071–3073.
[14] B.C. Stuart, M.D. Feit, S. Herman, A.M. Rubenchik, B.W. Shore, M.D. Perry, Phys. Rev. B 53 (1996) 1749–1761.
[15] M. Lenzner, J. Kruger, S. Sartania, Z. Cheng, C. Spielmann, G. Mourou, W. Kautek, F. Krausz, Phys. Rev. Lett. 80 (1998) 4076–4079.
[16] M. Li, S. Menon, J. Nibarger, G. Gibson, Phys. Rev. Lett. 82 (1999) 2394–2397.
[17] M. Downer, R. Fork, C. Shank, J. Opt. Soc. Am. B 2 (1985) 595–599.
[18] S. Cahill, A. Rinzler, F. Owens, S. Bulusu, J. Phys. Chem. 98 (1994) 7095–7100.
[19] N. Fell, J. Widder, S. Medlin, J. Morris, R. Pesce-Rodriguez, K. McNesby, J. Ram. Spec. 27 (1996) 97–104.
[20] N. Garland, S. McElvany, Chem. Phys. Lett. 297 (1998) 147–153.
[21] J. Oxley, J. Smith, W. Zheng, E. Rogers, M. Coburn, J. Phys. Chem. A 101 (1997) 4375–4383.